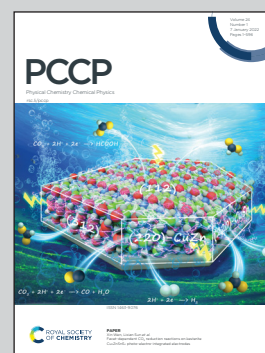**Showcasing work from the Germany-Japan research team by Profs. Dopfer, Mitric, Miyazaki and Fujii**

Real-time observation of photoionization-induced water migration dynamics in 4-methylformanilide–water by picosecond time-resolved infrared spectroscopy and *ab initio* molecular dynamics simulations

A novel time-resolved pump-probe spectroscopic approach that keeps high resolution in both the time and energy domain, nanosecond excitation–picosecond ionization–picosecond infrared probe spectroscopy, has been applied to the *trans*-4-methylformanilide–water cluster. Water migration dynamics from the CO to the NH sites in a peptide linkage triggered by photoionization is directly monitored by the ps time evolution of IR spectra. A significant acceleration of water migration has been found by substitution of the methyl group.

ROYAL SOCIETY
OF **CHEMISTRY**

rsc.li/pccp

Check for updates

Real-time observation of photoionization-induced water migration dynamics in 4-methylformanilide–water by picosecond time-resolved infrared spectroscopy and *ab initio* molecular dynamics simulations†

Mitsuhiko Miyazaki, [ID] *[ab] Tairiku Kamiya,[b] Matthias Wohlgemuth, [ID] [c]
Kuntal Chatterjee, [ID] [d] Roland Mitrić, [ID] *[c] Otto Dopfer [ID] *[de] and Masaaki Fujii [ID] *[be]

A novel time-resolved pump–probe spectroscopic approach that enables to keep high resolution in both the time and energy domain, nanosecond excitation–picosecond ionization–picosecond infrared probe (ns–ps–ps TRIR) spectroscopy, has been applied to the *trans*-4-methylformanilide–water (4MetFA–W) cluster. Water migration dynamics from the CO to the NH binding site in a peptide linkage triggered by photoionization of 4MetFA–W is directly monitored by the ps time evolution of IR spectra, and the presence of an intermediate state is revealed. The time evolution is analyzed by rate equations based on a four-state model of the migration dynamics. Time constants for the initial to the intermediate and hot product and to the final product are obtained. The acceleration of the dynamics by methyl substitution and the strong contribution of intracluster vibrational energy redistribution in the termination of the solvation dynamics is suggested. This picture is well confirmed by the *ab initio* on-the-fly molecular dynamics simulations. Vibrational assignments of 4MetFA and 4MetFA–W in the neutral (S_0 and S_1) and ionic (D_0) electronic states measured by ns IR dip and electron-impact IR photodissociation spectroscopy are also discussed prior to the results of time-resolved spectroscopy.

1. Introduction

Realignment of solvent molecules is an initial process of chemistry in solution, and it significantly affects the reaction rates and yields.[1–3] Thus, the solvation dynamics after photo-excitation of a solute molecule has attracted strong attention, even from the early stage of ultrafast spectroscopy.[4–6] For biomolecules, hydration dynamics around proteins is one of the most important dynamical processes because the biological

functions of proteins take place in water, and the surfaces of proteins are usually covered by water molecules. Protein folding obviously triggers rearrangement of surrounding water molecules.[7–10] Protein transport is also strongly dependent on how tightly bound the surrounding water molecules are. Due to their importance, water molecules surrounding proteins are often called "biological water".[11,12]

The dynamics of biological water has been interrogated by several methods such as NMR spectroscopy, neutron scattering, and dynamic Stokes shifts.[13–18] However, the interpretation of these studies on dynamics of biological water in solution are often controversial,[8,19] and the lifetime of initial dynamical processes of biological water spreads over the sub-nanosecond to picosecond range.[13,14] This discrepancy may be due to the fact that biological water is inhomogeneous, and each of the above experimental techniques probes the dynamics of water molecules in different environments. A recent review about biological water describes this unfortunate situation by the famous poem of John Godfrey Saxe "The Blind Men and the Elephant".[19]

To circumvent the problem of inhomogeneous water molecules, we have been working on hydration dynamics at a

[a] *Natural Science Division, Faculty of Core Research, Ochanomizu University, 2-1-1 Ohtsuka, Bunkyo-ku, Tokyo 112-8610, Japan. E-mail: miyazaki.mitsuhiko@ocha.ac.jp*

[b] *Laboratory for Chemistry and Life Science, Institute of Innovative Research, Tokyo Institute of Technology, Yokohama 226-8503, Japan*

[c] *Institut für Physikalische und Theoretische Chemie, Julius-Maximilians-Universität Würzburg, 97074 Würzburg, Germany. E-mail: roland.mitric@uni-wuerzburg.de*

[d] *Institut für Optik und Atomare Physik, Technische Universität Berlin, 10623 Berlin, Germany. E-mail: dopfer@physik.tu-berlin.de*

[e] *World Research Hub Initiatives, Institute of Innovative Research, Tokyo Institute of Technology, 4259-R1-15, Nagatsuta-cho, Midori-ku, Yokohama 226-8503, Japan. E-mail: mfujii@res.titech.ac.jp*

† Electronic supplementary information (ESI) available: [DETAILS]. See DOI: 10.1039/d1cp03327a

This journal is © the Owner Societies 2022

Phys. Chem. Chem. Phys., 2022, **24**, 73–85 | 73

single solvent molecular level by probing solvated clusters in the gas phase using time-resolved infrared (TRIR) spectroscopy and advanced *ab initio* molecular dynamics (MD) simulations.[20–25] This approach offers size- and isomer-selectivity as well as full control over solvation structure and energy in the cluster. Hydrated clusters generated in a molecular beam consist of solute and water molecules. The clusters are isolated at low temperature and thus the initial geometry and number of solvent molecules in the clusters are precisely defined. As a result, we can directly watch single water migration dynamics without ambiguity. The dynamics is typically initiated by UV laser excitation/photoionization of the clusters, and migration of the water molecule is monitored by changes in the TRIR spectra at the picosecond (ps) time scale. This technique of UV-UV(')-IR ps time-resolved IR (ps-TRIR) spectroscopy combined with mass spectrometry has been successfully applied to a variety of monohydrated clusters, including the single water CO → NH migration around the peptide linkage in *trans*-acetanilide (tAA)[20,21] and *trans*-formanilide (tFA),[24] the CN → NH migration around 4-aminobenzonitrile,[22] and the NH → OH migration in 5-hydroxyindole.[25] Surprisingly, the lifetimes of these single water migrations vary over four orders of magnitude, ranging from 4 ps to 53 ns. This wide variety of the migration time-constants has been rationalized by the differences in excess energies and potential energy surfaces for both the initial and final binding sites, such as (a) repulsive → bound, (b) flat → bound, and (c) bound → bound.[23,25] The slow migration lifetime in the bound → bound potential surface in 5-hydroxyindole–water is well reproduced by RRKM theory, and thus the intracluster vibrational energy redistribution (IVR) is one of the key factors to understand the variety of the hydration dynamics at the molecular

level. Analysis of the fast migration regime relies mostly on MD simulations.

For example, the *ab initio* "on-the-fly" MD simulations reproduce the time-evolutions (TEs) obtained by the ps-TRIR spectra on monohydrated clusters of tAA and tFA (tAA–W and tFA–W), and visualize the migration trajectories of water as shown in Fig. 1.[21,24] The water migration in tFA$^+$–W(CO) (hereafter, W(CO) and W(NH) mean the water molecule bound to the CO and NH sites, respectively) triggered by photoionization of the aromatic chromophore proceeds in the molecular plane. The water molecule released from the initial CO binding site migrates toward the final NH site, but overshoots and moves like a large-amplitude damped pendulum around the NH destination site. This overshooting motion is settled down within around 10 ps by vibrational energy transfer to low-frequency intra-molecular vibrations of tFA$^+$.[24] The migration dynamics in the related tAA$^+$–W(CO) cluster has been also simulated, and the twice faster migration than in tFA$^+$–W is well reproduced (Fig. 1).[21] tAA is a methyl-substituted derivative of tFA and thus the faster migration can be rationalized by the effect of the CH$_3$ group. The CH$_3$ group provides low-energy vibrational levels due to its (hindered) internal rotation, which accelerates the IVR.[26] Another effect of CH$_3$ substitution is its direct interaction with the water migration because the pathway is now split into in-plane and out-of-plane paths in tAA$^+$–W due to steric hindrance. In either case, it is clear that IVR from inter- to intramolecular vibrations controls the migration dynamics. However, it is difficult to evaluate the importance of the two effects, namely the density of states and the steric interaction.

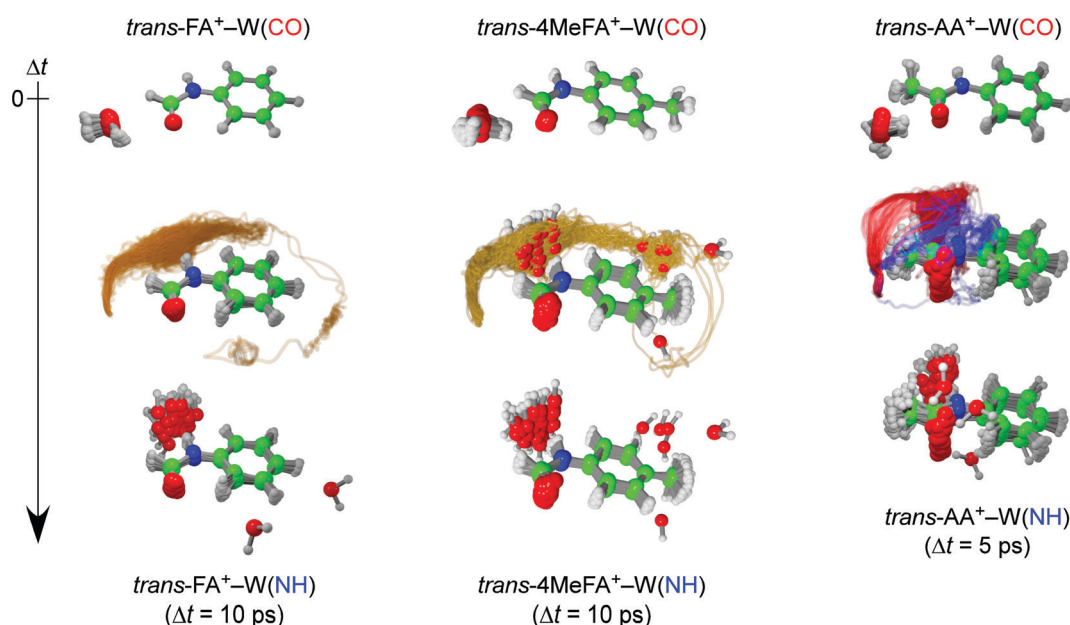In the present work, we apply ps-TRIR spectroscopy and *ab initio* MD simulation to the monohydrated clusters of

trans-FA$^+$–W(CO)   *trans*-4MeFA$^+$–W(CO)   *trans*-AA$^+$–W(CO)

trans-FA$^+$–W(NH)
(Δt = 10 ps)

trans-4MeFA$^+$–W(NH)
(Δt = 10 ps)

trans-AA$^+$–W(NH)
(Δt = 5 ps)

Fig. 1 Trajectories of the ionization-induced water migration derived from the *trans*-FA$^+$–W (left, 40 trajectories) and *trans*-AA$^+$–W (right, 50 trajectories) MD simulations, starting from the CO-bound isomer (top row) and ending at the NH-bound isomer (bottom row) at 10 and 5 ps after ionization, respectively (see movies in ESI†). The yellow curves for *trans*-FA$^+$–W indicate the in-plane migration path of water. The out-of-plane pathways for *trans*-AA$^+$–W correspond to the slow (blue) and fast (red) migration channels, respectively.

74 | *Phys. Chem. Chem. Phys.*, 2022, **24**, 73–85

This journal is © the Owner Societies 2022

trans-4-methylformanilide (4MetFA–W) to determine the effect of IVR acceleration by a CH_3 group. The ps-TRIR spectra and time evolutions are measured herein by a new spectroscopic approach, namely a nanosecond excitation–picosecond ionization–picosecond IR probe (ns–ps–ps) technique. An increased spectral resolution realized by replacement of the excitation laser from a ps to ns laser allows us to achieve a higher species-selectivity in ps-TRIR spectroscopy, which is crucial in cluster spectroscopy. The CH_3 group in 4MetFA is located at the remote *para*-position to the peptide linkage (–CONH–), and thus does not interfere with the water migration pathway. From the comparison to the dynamics of tFA^+–W, we can discuss the effect of the density of states on the single water migration dynamics.

2. Experimental and theoretical methods

2.1. Experimental

2.1.1. Stationary UV and IR spectroscopies. The stationary UV and IR spectroscopies were carried out by utilizing resonance-enhanced multiphoton ionization (REMPI) and double resonance IR-UV (IR dip and IR hole-burning) and UV-IR depletion schemes utilizing nanosecond lasers. Briefly, target molecules/clusters were ionized by REMPI *via* the $S_1 \leftarrow S_0$ origin transitions using two UV laser pulses for excitation and ionization (ν_{exc} and ν_{ion}). With a certain delay time (Δt) to the UV pulses, an IR laser pulse (ν_{IR}) was introduced ($\Delta t = -50$ ns for S_0, $\Delta t = +50$ ns for D_0). For measurements in the S_1 state, ν_{exc} and ν_{ion} were delayed *ca.* 10 ns, and ν_{IR} was introduced in between them to minimize temporal overlap among the pulses.

4MetFA (Tokyo Chemical Industry Co., LTD, >98%) was used without further purification. The sample of 4MetFA was put in a glass tube with molecular sieves and set in a holder behind a pulsed valve, both of which were heated to 343 K. Water was stored in a vessel located between the carrier gas cylinder and the valve, and cooled down to 243 K. Vapor of 4MetFA and water was seeded in He (1–2 bar), and the resulting mixture was expanded into vacuum through the pulsed valve.

The jet expansion was collimated by a skimmer ($\phi = 2$ mm) and introduced into the acceleration region of a time-of-flight mass spectrometer. The molecular beam was irradiated by the ns laser pulses, and the resulting ions were detected by a Daly detector at the end of the flight tube. Pulsed-field extraction was employed for introducing the ions into the flight tube to minimize field shifts in the ionization energy. The field shift of 14 cm^{-1} resulting from field ionization of Rydberg states was determined on the basis of the adiabatic ionization energy (IE_0) of phenol[27] recorded under the same condition. The ν_{exc} and ν_{ion} pulses were generated by second harmonic generation of dye laser outputs pumped by Nd:YAG lasers. The ν_{IR} pulse was obtained by difference-frequency generation as described elsewhere,[28,29] but the nonlinear crystal was changed from $LiNbO_3$ to KTA. Laser frequencies were calibrated to within ± 1 cm^{-1} by a wavemeter, while relative frequencies are determined to within ± 0.5 cm^{-1}. The ν_{exc} and ν_{ion} beams were

focused on the molecular beam by a lens with $f = 1500$ mm after adjusting focusing by telescopes equipped with a spatial filter. The ν_{IR} beam was introduced in a counter propagating manner to the UV pulses and focused by a BaF_2 lens with $f = 350$ mm.

2.1.2. Electron impact ionization (EI)-IR spectroscopy. EI-IR spectroscopy was carried out to obtain the IR spectrum of the most stable isomer of the $4MetFA^+$–W cation cluster. EI-IR spectra of size-selected clusters were recorded in a quadrupole–octopole–quadrupole tandem mass spectrometer coupled to an electron ionization source.[30,31] Clusters were generated in a pulsed supersonic plasma expansion by electron and/or chemical ionization of 4MetFA close to the nozzle orifice followed by aggregation/cooling, which produces predominantly the most stable cluster isomer in the cationic ground state (D_0). The expanding gas mixture was produced by passing Ar carrier gas (8–10 bar) through a reservoir filled with 4MetFA, which was heated to 418 K. Cluster ions of interest were mass-selected by the first quadrupole and subsequently irradiated with ν_{IR} from a tunable optical parametric oscillator pumped by a Nd:YAG laser. The IR laser frequency was calibrated to better than 1 cm^{-1} using a wavemeter. Resonant vibrational excitation induces the loss of the most-weakly bound ligand(s). Fragment ions produced by the IR absorption were mass-selected with the second quadrupole and monitored by a Daly detector. To separate the signal of laser-induced dissociation from the metastable decay background, the ion source was triggered at twice the laser frequency, and signals from alternating triggers were subtracted. To reduce the width of the transitions caused by internal energy of the cluster ions, tagging with loosely bound Ar was also performed.

2.1.3. TRIR spectroscopy. The nanosecond excitation–picosecond ionization–picosecond IR probe (ns–ps–ps) scheme (Fig. 2) was adopted to achieve a higher species-selectivity in ps-TRIR spectroscopy, which is restricted by the energy-time uncertainty relation. In this scheme, a population in a S_1 vibronic level is prepared by a ns UV pulse (ν_{exc} (ns)) as the first step. The population in this level is then ionized by a ps UV pulse (ν_{ion} (ps)) to trigger a reaction in the cationic D_0 state, and the population of the produced ion is monitored as ion current. The dynamics is traced by a ps IR pulse (ν_{IR} (ps)) with a certain delay time (Δt) from the ionization event through changes in the monitored ion population caused by resonant IR absorption. Coupling of the first ns excitation process offers a much better state selectivity for the subsequent ps pump–probe spectroscopy in the D_0 state, even for the case of a cluster system with a congested excitation spectrum resulting from close-lying or overlapping transitions of isomers and fragments from higher clusters, which is illustrated in Fig. S1 (ESI†) in detail.

The 4MetFA–W clusters were produced in a similar manner to that of the stationary spectroscopy but in a pulsed free jet expansion. The clusters were irradiated by laser pulses *ca.* 1 cm downstream from the pulsed valve, and resulting ions were turned by 90° into a quadrupole mass filter before the ion current in the $4MetFA^+$–W mass channel was detected by a channeltron. Picosecond laser pulses were generated by a

This journal is © the Owner Societies 2022

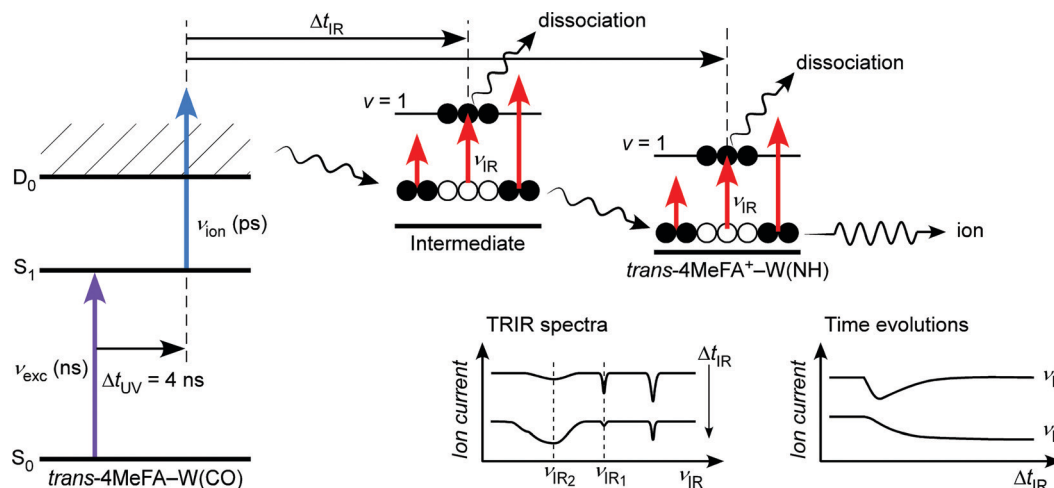*Phys. Chem. Chem. Phys.*, 2022, **24**, 73–85 | 75

Fig. 2 Excitation scheme of the ns excitation–ps ionization–ps IR time resolved spectroscopy. A single vibronic level in the excited state, which is prepared precisely by the ns excitation pulse (ν_{exc} (ns)), is ionized by ν_{ion} (ps) to trigger solvent dynamics in the cationic D_0 state, and the dynamics is probed by the tunable ν_{IR} (ps) pulse through time-resolved IR photodissociation spectroscopy.

high-energy ps laser setup described in detail elsewhere.[32–34] Briefly, tunable ps UV (ν_{ion} (ps)) and IR (ν_{IR} (ps)) pulses were generated through optical parametric and nonlinear frequency conversion processes of a ps pulse obtained from regenerative amplification of a femtosecond Ti/Sapphire laser pulse. The energy and time resolutions of the ν_{ion} (ps) and ν_{IR} (ps) pulses were *ca.* 12 cm^{-1} and 3 ps, respectively. The second harmonic of a ns dye laser pumped by a Nd:YAG laser was used as excitation UV pulse (ν_{exc} (ns)). These pulses were then combined by beam combiners and focused on the jet expansion by a CaF$_2$ lens with f = 300 mm after adjusting the focusing by telescopes. The delay time between the ps UV and IR pulses (Δt_{IR}) was controlled by optical delay stages. The delay between ν_{exc} (ns) and ν_{ion} (ps) (Δt_{UV}) was separated by *ca.* 4 ns (adjusted by a digital delay generator) to avoid unexpected photoprocesses caused by their overlap. This delay is shorter than the lifetime of the cluster measured as 13 ns (see Fig. S2 in ESI†).

2.2. Theoretical methods

Quantum chemical calculations were carried out at the CAM-B3LYP/aug-cc-pVTZ level of theory with the GD3BJ empirical dispersion correction using Gaussian16.[35] Relative energies (E_{rel}) of structural isomers of 4MetFA–W were evaluated including the (non-scaled) harmonic zero-point energy (ZPE) correction estimated from the normal mode analysis. The theoretical vibrational frequencies were scaled by 0.95 for comparison with experimental IR spectra.

In order to generate the initial conditions for the MD simulations of 4MetFA–W in the D_0 state, a 50 ps long trajectory in the S_1 excited electronic state at a constant temperature of T = 100 K was run employing the TD-CAM-B3LYP functional. This temperature is chosen to reproduce the experimental excess energy after photoionization and is the same as the one used for the tAA$^+$–W simulations. After initial equilibration, structures and velocities in regular time intervals were sampled, thus generating an ensemble of 50 initial conditions.

The MD simulations starting from these initial conditions were propagated for 10 ps in the D_0 cationic state. The integration of the classical equations of motions was performed using the velocity Verlet algorithm with a time step of 0.2 fs, which is sufficiently small to obtain adequate conservation of energy. At each step of the trajectories, electronic and nuclear dipole moments are calculated in order to serve as basis for simulating the ps-TRIR spectra. The latter are simulated according to the procedure that has been presented previously (for details see ref. 21, 24, 36 and 37). Briefly, the ps-TRIR spectrum is expressed as a trajectory average of the windowed Fourier transform of the dipole derivative function of each trajectory, where the probe pulse envelope serves as a window. The finite width of the pump pulse is obtained by convoluting the transient IR spectra with the experimental time resolution obtained from measuring the cationic state population of the NH isomer, which does not undergo any isomerisation dynamics. In the simulations, Gaussian-shaped laser pulses with the envelope of a FWHM of 3 ps were employed. The pulse widths correspond to the experimentally determined values.

3. Results and discussion

3.1. UV spectra

3.1.1. REMPI spectra. Fig. 3 shows 1 + 1′ 2-color REMPI spectra of 4MetFA and 4MetFA–W. The REMPI spectrum of 4MetFA in Fig. 3(A) reveals an intense band at 35 192 cm^{-1}, which is red-shifted by 812 cm^{-1} from the $S_1 \leftarrow S_0$ origin of tFA (36 004 cm^{-1}).[38–42] This red-shift is in line with shifts induced by CH$_3$ substitution at the *para*-position of mono-substituted benzenes as summarized in Table S1 (ESI†), and no other prominent band was observed below this transition. Thus, this band is assigned to the $S_1 \leftarrow S_0$ origin of 4MetFA. This assignment is confirmed by IR spectroscopy discussed in Section 3.2. From the analogy to tFA and tAA,[26,43–45] other weaker features are assigned to S_1 vibronic bands (Table 1).
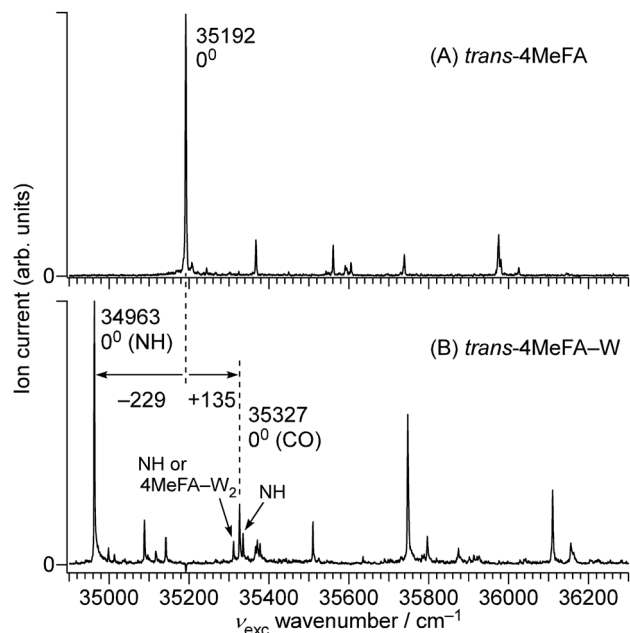
76 | *Phys. Chem. Chem. Phys.*, 2022, **24**, 73–85

This journal is © the Owner Societies 2022

PCCP

Paper

Fig. 3 $1 + 1'$ REMPI spectra of (A) *trans*-4MeFA and (B) *trans*-4MeFA–W obtained by ns lasers.

The complicated appearance of the REMPI spectrum of 4MetFA–W shown in Fig. 3(A) suggests the existence of several isomers. In the case of tFA, hydration occurs at either the NH or CO sites, and the S_1 origins are shifted by -218 and $+113$ cm^{-1} from the tFA monomer, respectively.[39–41] The REMPI spectrum of 4MetFA–W shows two pronounced bands shifted by -229 and $+135$ cm^{-1} from the origin band of the 4MetFA monomer.

Table 1 Transition frequencies and vibrational assignments of REMPI spectra of the *trans*-4MeFA and *trans*-4MeFA–W clusters

Species	ν_{obs}/cm^{-1}	ν_{vib}/cm^{-1}	Assignments[bcd]
trans-4MeFA	35 192	0	0^0
	35 207	15	$2e'_{Me\,rot}$
	35 244	52	$3a_1''_{Me\,rot}$ (?)
	35 367	175	β_{amide}
	35 561	369	$\nu_{18\,or\,16}$
	35 739	547	ν_{6b}
	35 975	783	ν_{12} or γ_{NH}
trans-4MeFA–W	34 963 $(-229)^a$	0	0^0 (NH)
	34 998	35	$2e'_{Me\,rot}$ (NH)
	35 013	50	$3a_1''_{Me\,rot}$ (NH)
	35 088	125	σ_{H_2O} (NH)
	35 142	179	β_{amide} (NH)
	35 327 $(+135)^a$	0	0^0 (CO)
	35 336	373	ν_{18} or ν_{16} (NH)
	35 371	407	? (NH)
	35 511	547	ν_{6b} (NH)
	35 748	785	ν_{12} or γ_{NH} (NH)
		833	? (NH)
		911	ν_1? (NH)
	36 111	784	ν_{12} or γ_{NH} (CO)
	36 156	829	? (CO)

^{a} Shift from the monomer 0^0 transition. ^{b} Wilson notation. ^{c} (NH) and (CO) mean the NH- and CO-bound isomers, respectively. The isomer assignment is assured from IR-UV hole-burning spectra. ^{d} The ? symbols indicate tentative or unknown vibrational assignments.

Thus, these features are attributed to the origin bands of the NH- and CO-bound isomers of 4MetFA–W, respectively. These assignments are confirmed below by IR and IR-UV hole-burning (IR-HB) spectroscopies. Major assignments including vibronic bands are summarized in Table 1.

The conformation of the amide group in FA keeps a small population in the *cis* form even under jet-cooled conditions.[40,42] The $S_1 \leftarrow S_0$ origin band of *cis*-FA (34 914 cm^{-1}) shows a red-shift of -1091 cm^{-1} from that of tFA (36 004 cm^{-1}) accompanied with a long progression arising from a change in planarity of the amide group.[40] The *cis*-4MeFA is also detected by REMPI spectroscopy as shown in Fig. S3 in ESI.† The spectrum shows much more complicated features than for *cis*-FA, probably due to coupling with the CH$_3$ internal rotation. The detection of *cis*-FA–W in a jet expansion was reported recently by microwave spectroscopy.[46] However, no transition assignable to *cis*-4MeFA–W was detected by REMPI spectroscopy in the present work. A much larger hydration-induced origin shift and/or some fast dynamics from the S_1 state for the *cis* isomers may be reasons for the absence in the investigated spectral range.

3.1.2. Photoionization efficiency (PIE) and photodissociation efficiency (PDE) spectra. To deduce the energetics of the hydration of 4MetFA, PIE and PDE spectra were measured *via* the respective S_1 origin bands (Fig. S4 and S5 in ESI†). PIE spectra of 4MetFA and 4MetFA–W(NH) demonstrate sharp steps at 65 135 and 62 167 cm^{-1} corresponding to their adiabatic ionization energies. These are field-corrected values, which was 14 cm^{-1} in the measurements. Appearance of the sharp steps means similarity of the structures between the S_1 and D_0 states. The red-shift of IE_0 (-2237 cm^{-1}) induced by the *p*-methyl substitution is consistent to other mono-substituted benzenes (see Table S2 in ESI†). On the other hand, the PIE spectrum of 4MetFA–W(CO) shows a gradual increase, and no clear step is seen. Thus, only an upper bound of IE_0, 64 800 cm^{-1}, was estimated from the position at which a detectable signal level could be obtained. The broad onset of the PIE spectrum is indicative of a large structural change upon ionization (including water migration) of 4MetFA–W(CO), similar to those observed for tFA–W(CO) and tAA–W(CO).

PDE spectra of 4MetFA–W(NH/CO) were recorded to determine the binding energies of the water ligand in a similar manner to that of PIE measurements by monitoring 4MetFA$^+$ produced from photodissociation of the clusters (Fig. S5 in ESI†). The binding energy was estimated only for 4MetFA–W(CO), while that of 4MetFA–W(NH) was not determined because no clear dissociation threshold was observed. Transition energies of 4MetFA and 4MetFA–W(NH/CO) obtained in this work are summarized in the energy diagram shown in Fig. 4. Corresponding values for tFA(–W) and tAA(–W) are compared in Fig. S6 (ESI†), and for a detailed discussion of this diagram, we refer to previous work.[23,47]

3.2. Stationary IR spectra

All stationary IR spectra measured in this study are compared in Fig. 5, including 4MetFA and 4MetFA–W in the S_0 (A–C), S_1 (D–F) and D_0 states (G, H). These spectra were obtained by IR

This journal is © the Owner Societies 2022
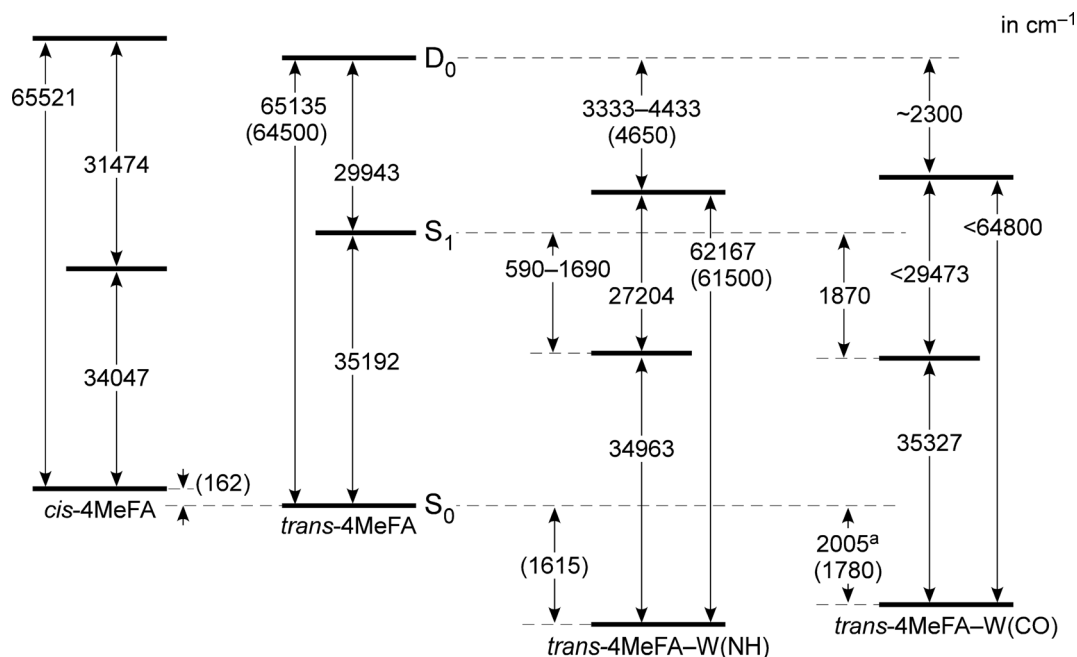
Phys. Chem. Chem. Phys., 2022, **24**, 73–85 | **77**

Fig. 4 Energy diagram of *cis/trans*-4MeFA and *trans*-4MeFA–W(NH/CO) clusters derived mostly from experimental values. Values in parentheses represent theoretical estimations (CAM-B3LYP/aug-cc-pVTZ). [a] The binding energy of water was estimated from the PDE spectrum.

dip spectroscopy. On the other hand, Fig. 5(I–L) show EI-IR spectra of 4MetFA$^+$–W, 4MetFA$^+$–W–Ar, and 4MetFA$^+$–Ar$_{1,2}$. Comparison with theoretical IR spectra is shown in Fig. S7 and S8 in the ESI.†

3.2.1. IR dip spectra in the S$_0$ state. IR dip spectra in the S$_0$ states show nearly the same appearance as those of tFA and tFA–W,[39] except for additional transitions arising from the additional CH$_3$ group. The similarity between the IR spectra of tFA and 4MetFA and their hydrated clusters means that the CH$_3$ group in the *para*-position does not have any significant effect on interactions around the amide group. Thus, the observed transitions are assigned as denoted in the figures (Table 2). The IR spectrum of *cis*-4MetFA was also recorded (Fig. S7 in the ESI†), though we do not discuss it in detail here.

Fig. 5(B and C) shows IR spectra of 4MetFA–W recorded by probing at the 34 963 and 35 327 cm^{-1} origin bands in the REMPI spectrum, respectively. They are assigned to 4MetFA–W(NH) and 4MetFA–W(CO) isomers according to the appearance of the hydrogen-bonded and free NH stretching bands (ν_{NH}^{HB} and ν_{NH}^{f}, respectively) consistent with the S$_1$ origin band shifts. IR-HB spectra shown in Fig. S9 in ESI† confirm that these bands are indeed the S$_1 \leftarrow$ S$_0$ origin transitions of these isomers, because they are the lowest-energy transitions in each spectrum.

3.2.2. IR dip spectra in the S$_1$ state. Fig. 5(D–F) shows IR dip spectra in the S$_1$ states recorded by exciting the S$_1 \leftarrow$ S$_0$ origin transitions. These spectra preserve the same features as those in the S$_0$ states, and band positions almost match with those of tFA and tFA–W in the S$_1$ states, respectively.[39] This observation means that the S$_1$ states keep the same structures as those in the S$_0$ states, and therefore that no dynamics of the water ligand occurs by excitation to the S$_1$ origin.

The observed bands and their assignments are summarized in the Table 3.

3.2.3 IR dip spectra in the D$_0$ state. Fig. 5(G and H) shows IR dip spectra of 4MetFA$^+$–W in the D$_0$ state ionized *via* the S$_1 \leftarrow$ S$_0$ origin bands of the NH and CO isomers, respectively. Both IR spectra closely resemble each other, even though different hydration isomers are ionized. The nearly identical IR spectra suggest that the structures of both isomers become the same 50 ns after ionization to the D$_0$ state. The structures in D$_0$ are assigned to 4MetFA$^+$–W(NH), because of the appearance of the free OH stretching vibrations ($\nu_{OH}^{\prime 1}$, $\nu_{OH}^{\prime 3}$) around 3700 cm^{-1} and the broad hydrogen-bonded NH stretching vibration (ν_{NH}^{HB}) around 3200 cm^{-1}, as well as the disappearance of the free NH stretching band (ν_{NH}^{f}). The observed bands and their assignments are summarized in Table 4. This assignment means that the water molecule in the CO-bound isomer migrates to the NH site after ionization. Such an ionization-induced hydration site switching has been reported for several mono-hydrated amides (tFA,[24,48,49] tAA,[20,21,50] N-(2-phenylethyl)acetamide)[51] and also for monohydrated 4-aminobenzonitrile,[22,52] 5-hydroxyindole,[25,53,54] tryptamine,[55] aminophenol,[56,57] and phenylglycine.[58] The isomerization dynamics is investigated in Section 3.3 by ps-TRIR spectroscopy.

3.2.4. Electron impact ionization (EI)-IR spectra in the D$_0$ state. Fig. 5(I) shows IR spectra of 4MetFA$^+$–W obtained by EI-IR spectroscopy, which predominantly probes the spectrum of the most stable isomer in the D$_0$ state.[30] The spectrum matches with the IR dip spectra in Fig. 5(G and H), confirming that the most stable hydration structure in D$_0$ is the NH-bound isomer. This result also means that the isomerization of water starting from the CO-site terminates at the most stable NH binding site in D$_0$.
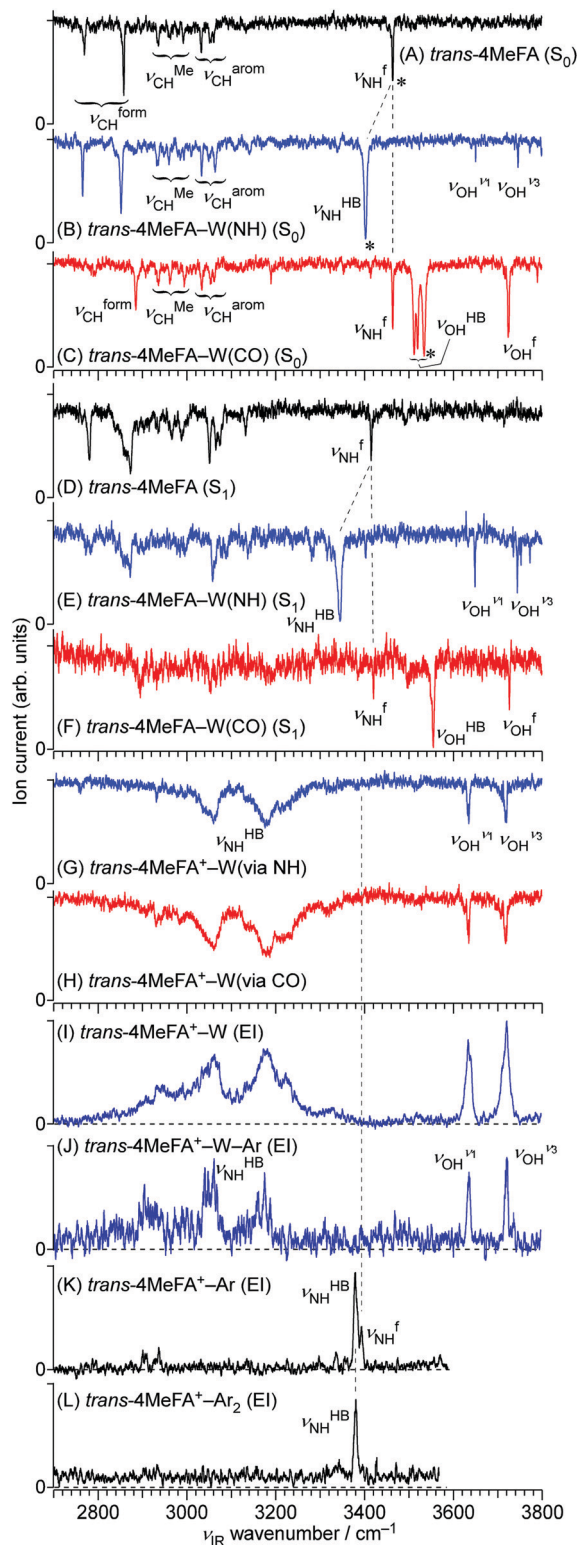
78 | *Phys. Chem. Chem. Phys.*, 2022, **24**, 73–85

This journal is © the Owner Societies 2022

Fig. 5 IR dip spectra of *trans*-4MeFA, *trans*-4MeFA−W(NH), and *trans*-4MeFA−W(CO) clusters in the S_0 states (A–C), *trans*-4MeFA, *trans*-4MeFA−W(NH), and *trans*-4MeFA−W(CO) clusters in the S_1 states (D–F), and *trans*-4MeFA⁺−W ionized *via* NH and CO bound clusters (G and H). Panels (I–L) show EI-IR spectra of *trans*-4MeFA⁺−W, *trans*-4MeFA⁺−W−Ar, *trans*-4MeFA⁺−Ar, and *trans*-4MeFA⁺−Ar₂. Asterisks in panels (A–C) represent bands used by IR-HB spectroscopy. ν_{ion} for measurement of the spectra (G and H) was fixed at 30 295 cm⁻¹.

Table 2 Infrared bands and assignments of 4MeFA and 4MeFA−W in the S_0 state

	ν_{CH}^{CHO}	ν_{CH}^{Me}	ν_{CH}^{arom}	ν_{NH}^{HB}	ν_{NH}^{f}	ν_{OH}^{HB}	ν_{OH}^{f}
trans-4MeFA	2770[a]	2936	3033	—	3463	—	—
	2859[a]	2962	3053				
		2993	3061				
cis-4MeFA	2871	2934	3035	—	3441	—	—
		2963	3062				
		2996					
trans-4MeFA−W(NH)	2766[a]	2934	3033	3402	—	—	3650 (ν_1)
	2852[a]	2960	3050				3745 (ν_3)
		2985	3063				
		2993					
trans-4MeFA−W(CO)	2792[a]	2936	3035	—	3464	3512[a]	3724
	2886[a]	2963	3054			3520[a]	
		2995	3062			3534[a]	

[a] Splitting due to anharmonic coupling.

Table 3 Infrared bands and assignments of 4MeFA and 4MeFA−W in the S_1 state

Species	ν_{CH}^{CHO}	ν_{CH}^{Me}	ν_{CH}^{arom}	ν_{NH}^{HB}	ν_{NH}^{f}	ν_{OH}^{HB}	ν_{OH}^{f}
trans-4MeFA	2780[a]	2935	3051	—	3415	—	—
	2860[a]	2966	3065				
	2873[a]	2988	3074				
trans-4MeFA−W(NH)	2782[a]	2996	3058	3344	—	—	3649 (ν_1)
	2858[a]		3088				3744 (ν_3)
	2873[a]						
trans-4MeFA−W(CO)	2894	2932	3052	—	3420	3555	3726

[a] Splitting due to anharmonic coupling.

Fig. 5(K and L) shows EI-IR spectra of 4MetFA⁺–Ar₁,₂. Ar tagging enables us to probe vibrational spectra of the monomer cation, for which single-photon IRPD does not work. Also, attachment of weakly-bound Ar atom(s) reduces the internal energy of the cation, and definite band positions can be determined by avoiding influences from hot bands. These spectra are again nearly identical to those of tFA⁺–Ar₁,₂,[59] reflecting the negligible perturbation of the CH₃ group in the *para*-position on the amide vibrations. The NH stretching vibration appears at 3380–3390 cm⁻¹ as a doublet reflecting the two possible binding sites for Ar. The higher frequency component stems from ν_{NH}^{f} of the π-bound isomer, in which Ar sticks on the aromatic ring, while the lower one arises from ν_{NH}^{HB} of the NH-bound isomer, in which Ar is hydrogen-bonded to the NH group.[59,60] The ν_{NH}^{f} band disappears in 4MetFA⁺–Ar₂ because the most stable NH binding site is occupied by one of the Ar atoms (the other sits on the π ring).

3.2.5. IR hole-burning (IR-HB) spectra. Using IR transition(s) specific to individual species, IR-UV hole-burning spectroscopy was performed to confirm the number of isomers present in the jet expansion, and to extract vibronic bands belonging to each isomer. IR transitions marked by asterisks in Fig. 5A–C were used to probe (burn) species, and REMPI spectra were recorded. Obtained spectra are compared with REMPI spectra in Fig. S9 (ESI†). The hole-burning spectrum of 4MetFA reproduces all bands in the REMPI spectrum, indicating that a

This journal is © the Owner Societies 2022

Phys. Chem. Chem. Phys., 2022, **24**, 73–85 | 79

Table 4 Infrared bands and assignments of 4MeFA, 4MeFA–W, and 4MeFA–W–Ar in the D_0 state

Species	$\nu_{CH}^{CHO\,b}$	$\nu_{CH}^{Me\,b}$	ν_{CH}^{arom}	ν_{NH}^{HB}	ν_{NH}^{f}	ν_{OH}^{HB}	ν_{OH}^{f}
trans-4MeFA$^+$–Ar (EI-IR)	2937 (?)	2903 (?)		3378 (NH-bound)	3393 (π-bound)		
trans-4MeFA$^+$–W (*via* NH)		2931 (?)		3060^a	—	—	3634 (ν_1)
				3180^a			3718 (ν_3)
				3215^a			
trans-4MeFA$^+$–W (*via* CO)		2932 (?)		3060^a			3634 (ν_1)
				3180^a			3717 (ν_3)
				3215^a			
trans-4MeFA$^+$–W–Ar (EI-IR)		2915^a		3150^a			3634 (ν_1)
				3175^a			3719 (ν_3)

^{a} Fermi resonance multiplets arising from anharmonic coupling of strongly IR active NH fundamental and overtones. ^{b} The ? symbols indicate tentative assignments.

single conformation contributes to the REMPI spectrum in this range.

Transitions observed in the IR-UV hole-burning spectra of 4MetFA–W(NH/CO) reproduce the total REMPI spectrum, confirming that the two isomers are the only species observed in the jet expansion. From the lowest transition of each spectrum, the $S_1 \leftarrow S_0$ origin transitions of the NH/CO bound clusters are determined to be 34 963 and 35 327 cm^{-1}, respectively, as deduced from the shifts from that of the monomer. Major vibronic features are tentatively assigned in Table 1.
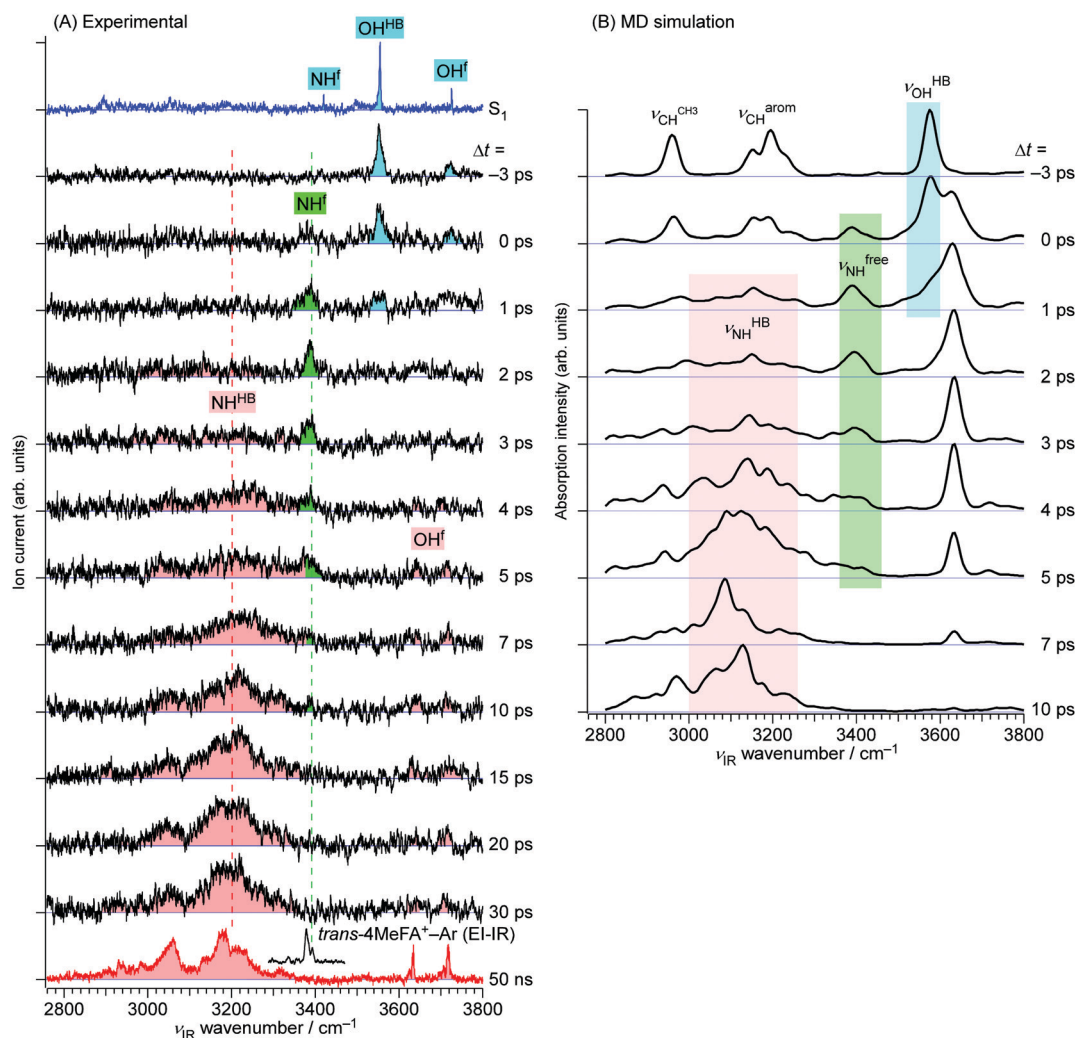

Fig. 6 (A) The ps-TRIR spectra of *trans*-4MeFA$^+$–W recorded by the ns-excitation–ps-ionization scheme. ν_{ion} was fixed to 33 213 cm^{-1}. The top and bottom traces show ns stationary IR spectra in the S_1 and D_0 states, respectively. The EI-IR spectrum of *trans*-4MeFA$^+$–Ar is also shown above the D_0 spectrum to indicate the ν_{NH}^{f} position of bare *trans*-4MeFA$^+$. (B) Theoretical TRIR spectra obtained by the *ab initio* on-the-fly MD simulations (see Section 4).

80 | *Phys. Chem. Chem. Phys.*, 2022, **24**, 73–85

This journal is © the Owner Societies 2022

3.3. Picosecond time-resolved IR spectroscopy

3.3.1. ps-TRIR spectra. Fig. 6 shows ps-TRIR spectra obtained by ionizing 4MetFA–W(CO) *via* the $S_1 \leftarrow S_0$ origin. Before ionization ($\Delta t < 0$), a strong band at 3555 cm^{-1} and a weak band at 3726 cm^{-1} appear, which are assigned to ν_{OH}^{HB} and ν_{OH}^{f} in the S_1 state by comparison to the stationary IR spectra in the S_1 state (Fig. 5(F)), which is reproduced at the top of Fig. 6. Immediately after the ionization event, the S_1 state features (ν_{OH}^{HB} and ν_{OH}^{f}) disappear, and instead, a new band comes up at 3393 cm^{-1}. This band position matches with that of ν_{NH}^{f} of 4MetFA$^+$ obtained from the EI-IR spectrum of 4MetFA$^+$–Ar (Fig. 5(K)) and reproduced in the second bottom panel of Fig. 6 for comparison. After $\Delta t > \sim 5$ ps, the ν_{NH}^{f} band gradually decreases in intensity, and a broad feature centered at ~ 3200 cm^{-1} grows. This broad absorption corresponds to ν_{NH}^{HB} of the NH-bound structure. After 15 ps, the ps-TRIR spectra do not change anymore, and the water molecule seems to have reached a final stationary state, the NH-bound structure.

The ps-TRIR spectra prove that the O–H$\cdots$O=C hydrogen bond is cleaved by ionization, and the water molecule starts the isomerization. This process is caused by the strong repulsion between the created positive charge of the cation and the partial positive charges on the water hydrogens. The ps-TRIR spectra also illustrate the existence of an intermediate during the course of the isomerization process of the water ligand, because ν_{NH}^{f} appears right after ionization and disappears after 10 ps, while ν_{NH}^{HB} continuously grows after 3 ps. This assignment of the intermediate means that the water molecule is released from the initial CO site but has not yet arrived at the final NH site in 4MetFA$^+$.

3.3.2. Time evolutions (TEs). The TEs of the ν_{NH}^{f} (3393 cm^{-1}) and ν_{NH}^{HB} (3200 cm^{-1}) vibrations in the ps-TRIR spectra were traced to reveal dynamics of the hydration site switching, and they are plotted in Fig. 7(A) and (B), respectively. The ν_{NH}^{f} band, which represents the population of the intermediate, appears at $\Delta t = 0$ (ionization event) and immediately decays until $\Delta t \sim 15$ ps, while ν_{NH}^{HB} gradually rises with the corresponding rate of the ν_{NH}^{f} decay. This observation directly proves that the water molecule is transferred from the CO site to the NH site after ionization through an intermediate within ~ 15 ps.

This behavior of the TEs is quite similar to those of tFA$^+$–W and tAA$^+$–W, both of which show water migration motions with an intermediate.[20,21,24] The structures of the intermediates, however, are different depending on the migration pathways. In the case of tFA$^+$–W, the water molecule travels along an in-plane path around the CHO group, while in tAA$^+$–W it can take two competing pathways. One is an in-plane path similar to that of tFA$^+$–W, while the other is out-of-plane *via* an intermediate above the amide group.[20,21] These migration mechanisms were concluded through fruitful combination between the experimental observations and *ab initio* MD simulations. The determination of the rate constants of the observed dynamics in 4MetFA$^+$–W by a kinetic analysis requires a reaction model for the water migration process. Thus, we again deduced the migration model with the help from the *ab initio* MD simulation discussed in detail in Section 4.
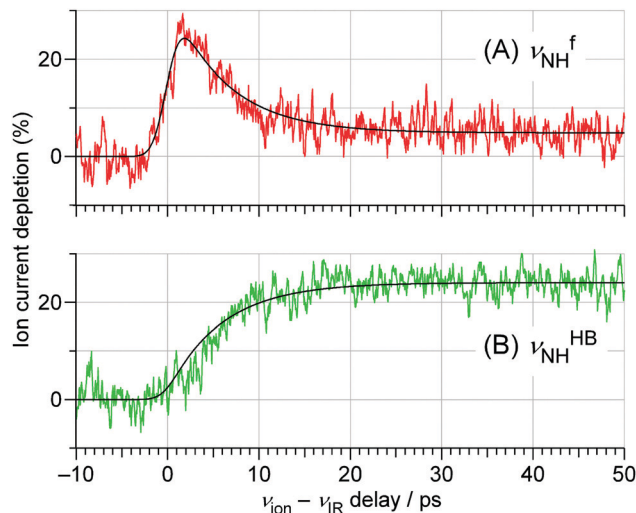

Fig. 7 TEs probed at the (A) ν_{NH}^{f} (3393 cm^{-1}) and (B) ν_{NH}^{HB} (3200 cm^{-1}) vibrations of *trans*-4MeFA$^+$–W obtained by the ns-excitation–ps-ionization scheme (Fig. 6). The best fits obtained by the kinetic analysis are also shown. The background signal in (A) after 30 ps arises from the tail of the strong ν_{NH}^{HB} band. See Section S-13 in ESI† for the detained explanation of the fitting model.

3.4. Kinetic analysis of TEs

3.4.1. Reaction model. Fig. 8 shows the kinetic model used for the analysis of the dynamics observed for 4MetFA$^+$–W. The model is based on four states proposed by the MD simulations. The water migration starts from the CO site of the CO-bound structure, the initial state (reactant R$^+$). It is generated by ionization from the S_1 state, which has the same CO-bound structure as the S_0 state. The water molecule is repelled after ionization from the CO site into the in-plane isomerization path around the formyl (CHO) group toward the NH site. After the NH site has been reached for the first time, the water molecule passes over the NH site due to its large translational energy. Then, it oscillates around the NH site until the translational energy is lost by IVR, which distributes the excess kinetic energy among low-frequency inter- and intramolecular vibrations. This damped oscillating state is represented in the model by two intermediates, a hot NH-bound structure (P$^+$(Hot)) and a hot NH-free structure (I$^+$), which are assumed to be in equilibrium. The final product state (P$^+$(Cold)) is the cold NH-bound structure formed when the translational energy is reduced down to below the barrier for the well at the NH site. Thus, the model is expressed in total by four states, the initial reactant, two intermediates, and the final product.

The initial state corresponds to the Franck–Condon (FC) state of ionization from the S_1 origin, and has the ν_{NH}^{f} of 4MetFA$^+$ as characteristic mode, but its contribution to the ps-TRIR spectra is low due to its short lifetime. Thus, the ν_{NH}^{f} band consists mainly of the intermediate of the hot NH-free structure (I$^+$). The hot NH-bound intermediate (P$^+$(Hot)) and the cold NH-bound product (P$^+$(Cold)) both contribute to ν_{NH}^{HB}. Their band positions and intensities are somewhat different

This journal is © the Owner Societies 2022

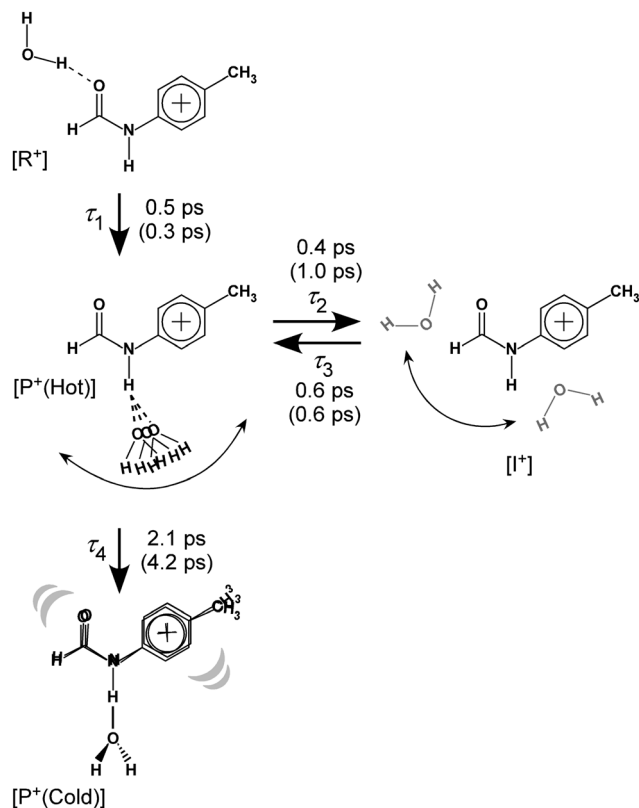*Phys. Chem. Chem. Phys.*, 2022, **24**, 73–85 | **81**

Fig. 8 Reaction model used for the kinetic fits of the TEs and resulting time constants. Values in parentheses represent those for *trans*-FA⁺−W discussed in detail in Fig. S10 and S11 (ESI†). See Section S-13 in ESI† for the detained explanation of the rate equations.

because of their different effective hydrogen bond strength. However, the extensive broadening of the ν_{NH}^{HB} band makes them indistinguishable in the experiment. The reaction time constants between these four states of the model are represented by τ_1–τ_4 (Fig. 8). The TEs were fitted by functions derived from the rate equations, details of which are given in the ESI.† In the fitting, functions are convoluted by a Gaussian with a FWHM of 2.8 ps, which represents the time response of the measurement.

3.4.2. Results of fits. The best fits of the model are compared in Fig. 7 to the experimental TEs, and the parameters are given in Table 5. The fits reproduce the experimental TEs well, suggesting that the reaction model contains the essential states of the water migration dynamics. The time constant τ_1 is much shorter than the instrumental resolution. This fast dynamics corresponds to the immediate formation of the intermediates, being consistent with the strong initial repulsion between the water molecule and the generated cation. The time constants $\tau_{2,3}$ for interconversion of the intermediates are also comparable to the instrumental resolution, and thus we do not discuss the differences of these constants in detail. Comparison of the more significant and reliable τ_4 constant of 4MetFA with tFA will be discussed in the next section.

3.4.3. Comparison to tFA–W. In this work, the ionization-induced water migration dynamics in tFA⁺−W and tAA⁺−W were

Table 5 Time-constants (in ps) obtained from the kinetic fits to the reaction model. See Section S-13 in ESI for the detained explanation of time constants in the rate equations. The errors of the values are estimated to be ±0.5 ps

Time constant	*trans*-4MeFA⁺–W	*trans*-FA⁺–W
τ_1	0.5	0.3
τ_2	0.4	1.0
τ_3	0.6	0.6
τ_4	2.1	4.2

re-measured by the ns-excitation–ps-ionization TRIR spectroscopy to directly compare the results on the same basis. The obtained ps-TRIR spectra and TEs are given in Fig. S10 and S11 (ESI†), respectively. The ps-TRIR spectra reproduce previous measurements well,[20,21,24] however with a better spectral quality. The time constants obtained from the kinetic fits to the TEs are compared in Table 5 for tFA⁺ and 4MetFA⁺. The case of tAA⁺ is not included because of its different reaction model.

The time constants τ_1–τ_3 are similar for 4MetFA⁺–W and tFA⁺–W, confirming also similar initial migration dynamics in both clusters. Indeed, the MD simulations predict similar in-plane paths around the CHO group with overshooting at the NH site. The time constants reveals however a marked shortening of τ_4 for 4MetFA⁺–W from 4.2 to 2.1 ps, indicating faster translational cooling of the water molecule at the NH site by IVR. This acceleration of IVR can be attributed to an increased vibrational density of states (vDOS) in 4MetFA⁺ arising from the additional CH₃ group. The anharmonic coupling between the in-plane motion of the water molecule and the NH group in tFA⁺/4MetFA⁺ is assumed to be the same because of the remote *para*-substitution of the CH₃ group.

To estimate the influence of the vDOS on the IVR rate, Fig. 9 compares the vDOSs of 4MetFA⁺–W, tFA⁺–W, and tAA⁺–W *versus* internal vibrational energy. The vDOSs were evaluated from differentiation of the smoothed curve of the total number of vibrational states obtained by integrating the number of vibrational states (vNOS) at each vibrational energy. vNOS was calculated using direct counting of the unscaled harmonic vibrational states obtained by the DFT calculations at a given vibrational energy by the Beyer–Swinehart algorithm.[61] The internal rotation of the CH₃ group was treated separately as a one-dimensional hindered rotation with an effective rotational constants of 5.2 cm⁻¹ on the internal rotation potential (without ZPE correction) obtained by relaxed scans at the same theoretical level. The rotational potentials and energy levels are shown in Fig. S12 in ESI.† Contributions from rotational states were neglected because the differences in rotational constants are small for the structures concerning the isomerization. From their IEs and photon energies used for ionization, the internal vibrational energies of the cluster cations are expected to be in the range of 3000 to 5000 cm⁻¹. In this excess energy range, vDOS of 4MetFA⁺–W is *ca.* 80 times higher than that of tFA⁺–W. This is significantly higher than the observed enhancement of IVR rate ($1/\tau_4$) by a factor 2. The higher vDOS in 4MetFA⁺ arises not only from the free rotational levels but also from other low-
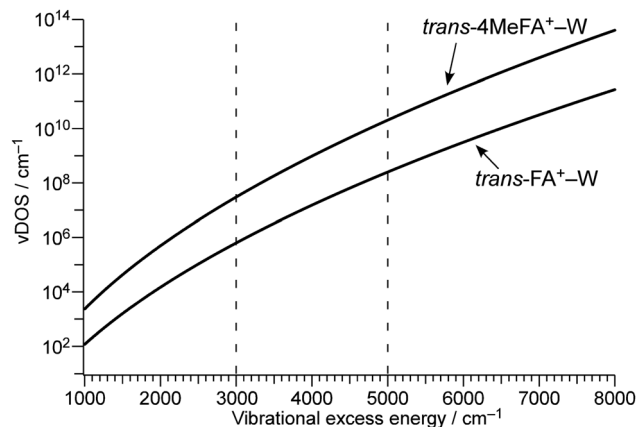
82 | *Phys. Chem. Chem. Phys.,* 2022, **24**, 73–85

This journal is © the Owner Societies 2022

Fig. 9 Vibrational excess energy dependence of vibrational density of states (vDOS) of *trans*-4MeFA$^+$–W and *trans*-FA$^+$–W. In *trans*-4MeFA$^+$–W, contributions from the CH$_3$ internal rotation are estimated regarding the CH$_3$ groups as independent rotors. Dashed lines indicate the excess energy range (3000–5000 cm^{-1}) of the product P$^+$ after photoionization.

frequency vibrations associated with the CH$_3$ group, such as its bending vibrations. Actually, contributions from these vibrations account for ∼40% of the increase in vDOS, meaning that the existence of the CH$_3$ group itself is essential for the higher density of low-frequency bath modes. Symmetry restriction due to the nuclear spin statistics of the CH$_3$ group reduce the effective vDOS. However, the difference between vDOS and the observed increase in the IVR rate is difficult to be rationalized only by the symmetry restriction. From the view point of the tier model (Fig. S14, ESI†),[62] the methyl substitution at the *para* position mainly increases the density of the second tier in the bath, while the doorway states in tFA$^+$–W and 4MetFA$^+$–W are similar. Thus, the acceleration of IVR occurs only from the second tier, and thus the effective IVR enhancement is reduced compared to the increase in vDOS.

4. *Ab initio* on-the-fly MD simulations

The MD simulations show that the water isomerization in 4MetFA–W proceeds along the same in-plane reaction pathway as in the case of tFA$^+$–W (Fig. 1 and the movie in ESI†).[24] In the simulation, the NH site is reached after 500 fs for the first time. The water molecule moves over to the opposite side of the phenyl ring, but finally stabilizes near the final destination, *i.e.*, the NH site in both systems. No out-of-plane migration, which is dominant in tAA$^+$–W, is found.[20,21]

The simulated TR-IR spectra based on the MD simulations are presented in Fig. 6B. The marker bands of the water migration dynamics, ν_{OH}^{HB}, ν_{NH}^{free}, and ν_{NH}^{HB} for the initial structure, the intermediate, and the final product are indicated in blue, green, and red color, respectively. The decrease of the ν_{OH}^{HB} band, the appearance and disappearance of the intermediate, and the rise of the final product are qualitatively well reproduced.

In order to analyze the influence of the CH$_3$ group on the energy redistribution dynamics, we consider the calculated
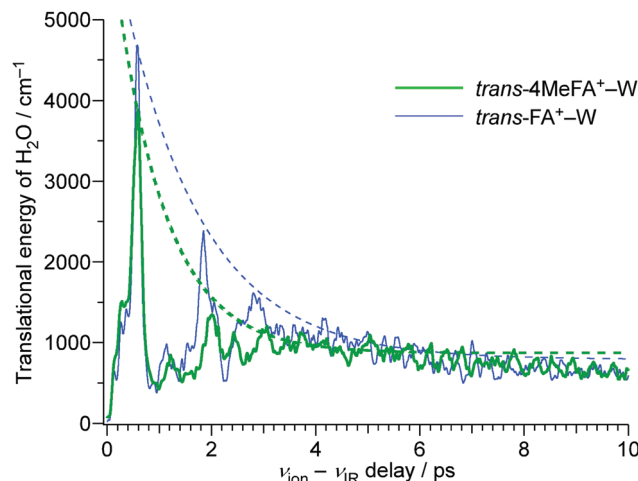

Fig. 10 Time profiles of the kinetic energy change in the water molecule of the *trans*-4MeFA$^+$–W and *trans*-FA$^+$–W obtained by the MD simulation. Single exponential curves representing the decay of the energy are shown as dashed lines. The damping time constants are 0.96 ps for 4MetFA$^+$–W and 1.53 ps for tFA$^+$–W.

average kinetic energies of the water molecule for the translational motion along the reaction coordinate (Fig. 10). Both tFA$^+$–W and 4MetFA$^+$–W exhibit a fast initial rise of the translational kinetic energy, which reaches a maximum around Δt = 500 fs followed by damped oscillations. The damping constant is significantly shorter for 4MetFA$^+$–W (0.96 ps) than for tFA$^+$–W (1.53 ps). The fast damping of the kinetic energy in 4MetFA$^+$–W is consistent with the fast IVR as already concluded from the observed time evolution. From the reasonable reproduction of the observed time-resolved spectra of 4MetFA$^+$–W, the effect of the CH$_3$ group on the acceleration of the water migration based on IVR is confirmed.

5. Summary

Water migration dynamics induced by photoionization of 4MetFA–W is revealed by the novel ns–ps–ps TRIR spectroscopy approach, which enables both the highly specific selection of the species at high spectral resolution and a sufficiently high time resolution in the ps part. The acceleration of the dynamics by the methyl group is clearly shown by comparison to the ps-TRIR spectra of tFA$^+$–W. The time evolution is analyzed by rate equations based on the four-state model of the migration dynamics. The strong contribution of IVR in the termination of the solvation dynamics is demonstrated. This picture is well reproduced by the *ab initio* on-the-fly MD simulations. Thus, acceleration of the dynamics by the methyl group and its relation to IVR are confirmed.

From the energetics, the driving force of the water migration, *i.e.* hydration dynamics at the single molecular level, originates from the initial water···cation repulsion and the stabilization at the final solvation site by the water···NH hydrogen bond. The kinetics of the migration motion is predominantly controlled by the energy randomization process in the cluster.

These results point out that both solvent–solute interaction and solute-bath energy flow must be carefully considered in the microscopic description. It demonstrates the advantage of the application of ps-TRIR spectroscopy to solvated clusters for the study of solvation dynamics at the molecular level, which is still challenging in the condensed phase.

Conflicts of interest

There are no conflicts to declare.

Acknowledgements

References

1 N. Mataga, H. Chosrowjan and S. Taniguchi, *J. Photochem. Photobiol., C*, 2005, **6**, 37–79.

2 M. Maroncelli, J. Macinnis and G. R. Fleming, *Science*, 1989, **243**, 1674–1681.

3 M. B. Smith, *March's advanced organic chemistry: reactions, mechanisms, and structure*, John Wiley & Sons, 2020.

4 M. M. Karelson and M. C. Zerner, *J. Phys. Chem.*, 1992, **96**, 6949–6957.

5 G. R. Fleming and M. Cho, *Annu. Rev. Phys. Chem.*, 1996, **47**, 109–134.

6 W. P. de Boeij, M. S. Pshenichnikov and D. A. Wiersma, *Annu. Rev. Phys. Chem.*, 1998, **49**, 99–123.

7 F. Persson, P. Söderhjelm and B. Halle, *J. Chem. Phys.*, 2018, **148**, 215101.

8 F. Persson, P. Söderhjelm and B. Halle, *J. Chem. Phys.*, 2018, **148**, 215103.

9 M.-C. Bellissent-Funel, A. Hassanali, M. Havenith, R. Henchman, P. Pohl, F. Sterpone, D. v. d. Spoel, Y. Xu and A. E. Garcia, *Chem. Rev.*, 2016, **116**, 7673–7697.

10 M. S. Cheung, A. E. Garcia and J. N. Onuchic, *Proc. Natl. Acad. Sci. U. S. A.*, 2002, **99**, 685–690.

11 B. Bagchi, *Chem. Rev.*, 2005, **105**, 3197–3219.

12 D. Zhong, S. K. Pal and A. H. Zewail, *Chem. Phys. Lett.*, 2011, **503**, 1–11.

13 S. K. Pal and A. H. Zewail, *Chem. Rev.*, 2004, **104**, 2099–2123.

14 S. M. Bhattacharyya, Z.-G. Wang and A. H. Zewail, *J. Phys. Chem. B*, 2003, **107**, 13218–13228.

15 L. Nilsson and B. Halle, *Proc. Natl. Acad. Sci. U. S. A.*, 2005, **102**, 13867–13872.

16 N. Nandi, K. Bhattacharyya and B. Bagchi, *Chem. Rev.*, 2000, **100**, 2013–2045.

17 X. J. Jordanides, M. J. Lang, X. Song and G. R. Fleming, *J. Phys. Chem. B*, 1999, **103**, 7995–8005.

18 N. V. Nucci, M. S. Pometun and A. J. Wand, *Nat. Struct. Mol. Biol.*, 2011, **18**, 245–250.

19 S. Mondal, S. Mukherjee and B. Bagchi, *J. Phys. Chem. Lett.*, 2017, **8**, 4878–4882.

20 K. Tanabe, M. Miyazaki, M. Schmies, A. Patzer, M. Schütz, H. Sekiya, M. Sakai, O. Dopfer and M. Fujii, *Angew. Chem., Int. Ed.*, 2012, **51**, 6604–6607.

21 M. Wohlgemuth, M. Miyazaki, M. Weiler, M. Sakai, O. Dopfer, M. Fujii and R. Mitrić, *Angew. Chem., Int. Ed.*, 2014, **53**, 14601–14604.

22 M. Miyazaki, T. Nakamura, M. Wohlgemuth, R. Mitrić, O. Dopfer and M. Fujii, *Phys. Chem. Chem. Phys.*, 2015, **17**, 29969–29977.

23 O. Dopfer and M. Fujii, *Chem. Rev.*, 2016, **116**, 5432–5463.

24 M. Wohlgemuth, M. Miyazaki, K. Tsukada, M. Weiler, O. Dopfer, M. Fujii and R. Mitrić, *Phys. Chem. Chem. Phys.*, 2017, **19**, 22564–22572.

25 M. Miyazaki, A. Naito, T. Ikeda, J. Klyne, K. Sakota, H. Sekiya, O. Dopfer and M. Fujii, *Phys. Chem. Chem. Phys.*, 2018, **20**, 3079–3091.

26 S. Ullrich and K. Müller-Dethlefs, *J. Phys. Chem. A*, 2002, **106**, 9188–9195.

27 S. Ullrich, G. Tarczay and K. Müller-Dethlefs, *J. Phys. Chem. A*, 2002, **106**, 1496–1503.

28 M. Miyazaki, J. Saikawa, H. Ishizuki, T. Taira and M. Fujii, *Phys. Chem. Chem. Phys.*, 2009, **11**, 6098–6106.

29 M. Miyazaki and M. Fujii, *Phys. Chem. Chem. Phys.*, 2017, **19**, 22759–22776.

30 O. Dopfer, *Z. Phys. Chem.*, 2005, **219**, 125–168.

31 O. Dopfer, *Int. Rev. Phys. Chem.*, 2003, **22**, 437–495.

32 S. Ishiuchi, M. Sakai, Y. Tsuchida, A. Takeda, Y. Kawashima, M. Fujii, O. Dopfer and K. Müller-Dethlefs, *Angew. Chem., Int. Ed.*, 2005, **44**, 6149–6151.

33 M. Sakai, S. Ishiuchi and M. Fujii, *Eur. Phys. J. D*, 2002, **20**, 399–402.

34 S. Ishiuchi, M. Sakai, K. Daigoku, T. Ueda, T. Yamanaka, K. Hashimoto and M. Fujii, *Chem. Phys. Lett.*, 2001, **347**, 87–92.

35 M. J. Frisch, G. W. Trucks, H. B. Schlegel, G. E. Scuseria, M. A. Robb, J. R. Cheeseman, G. Scalmani, V. Barone, G. A. Petersson, H. Nakatsuji, X. Li, M. Caricato, A. V. Marenich, J. Bloino, B. G. Janesko, R. Gomperts, B. Mennucci, H. P. Hratchian, J. V. Ortiz, A. F. Izmaylov, J. L. Sonnenberg, D. Williams-Young, F. L. F. Ding, J. G. F. Egidi, A. P. B. Peng, T. Henderson, D. Ranasinghe,

84 | *Phys. Chem. Chem. Phys.*, 2022, **24**, 73–85

This journal is © the Owner Societies 2022

V. G. Zakrzewski, J. Gao, N. Rega, G. Zheng, W. Liang, M. Hada, M. Ehara, K. Toyota, R. Fukuda, J. Hasegawa, M. Ishida, T. Nakajima, Y. Honda, O. Kitao, H. Nakai, T. Vreven, K. Throssell, J. J. A. Montgomery, J. E. Peralta, F. Ogliaro, M. J. Bearpark, J. J. Heyd, E. N. Brothers, K. N. Kudin, V. N. Staroverov, T. A. Keith, R. Kobayashi, J. Normand, K. Raghavachari, A. P. Rendell, J. C. Burant, S. S. Iyengar, J. Tomasi, M. Cossi, J. M. Millam, M. Klene, C. Adamo, R. Cammi, J. W. Ochterski, R. L. Martin, K. Morokuma, O. Farkas, J. B. Foresman and D. J. Fox, *Gaussian 16 Revision C.01*, Gaussian, Wallingford CT, 2016.

36 V. Bonačić-Koutecký and R. Mitrić, *Chem. Rev.*, 2005, **105**, 11–66.

37 R. Mitrić and V. Bonačić-Koutecký, *Phys. Rev. A: At., Mol., Opt. Phys.*, 2007, **76**, 031405.

38 M. Mons, I. Dimicoli, B. Tardivel, F. Piuzzi, E. G. Robertson and J. P. Simons, *J. Phys. Chem. A*, 2001, **105**, 969–973.

39 E. G. Robertson, *Chem. Phys. Lett.*, 2000, **325**, 299–307.

40 J. A. Dickinson, M. R. Hockridge, E. G. Robertson and J. P. Simons, *J. Phys. Chem. A*, 1999, **103**, 6938–6949.

41 A. V. Fedorov and J. R. Cable, *J. Phys. Chem. A*, 2000, **104**, 4943–4952.

42 V. P. Manea, K. J. Wilson and J. R. Cable, *J. Am. Chem. Soc.*, 1997, **119**, 2033–2039.

43 S. Ullrich and K. Müller-Dethlefs, *J. Phys. Chem. A*, 2002, **106**, 9181–9187.

44 S. Ullrich, G. Tarczay, X. Tong, C. E. H. Dessent and K. Müller-Dethlefs, *Phys. Chem. Chem. Phys.*, 2001, **3**, 5450–5458.

45 S. Ullrich, X. Tong, G. Tarczay, C. E. H. Dessent and K. Müller-Dethlefs, *Phys. Chem. Chem. Phys.*, 2002, **4**, 2897–2903.

46 P. Pinacho, S. Blanco and J. C. López, *Phys. Chem. Chem. Phys.*, 2019, **21**, 2177–2185.

47 M. Weiler, T. Nakamura, H. Sekiya, O. Dopfer, M. Miyazaki and M. Fujii, *ChemPhysChem*, 2012, **13**, 3875–3881.

48 T. Ikeda, K. Sakota, Y. Kawashima, Y. Shimazaki and H. Sekiya, *J. Phys. Chem. A*, 2012, **116**, 3816–3823.

49 K. Sakota, Y. Shimazaki and H. Sekiya, *Phys. Chem. Chem. Phys.*, 2011, **13**, 6411–6415.

50 K. Sakota, S. Harada, Y. Shimazaki and H. Sekiya, *J. Phys. Chem. A*, 2011, **115**, 626–630.

51 K. Sakota, S. Harada and H. Sekiya, *Chem. Phys.*, 2013, **419**, 138–144.

52 T. Nakamura, M. Schmies, A. Patzer, M. Miyazaki, S. Ishiuchi, M. Weiler, O. Dopfer and M. Fujii, *Chem. – Eur. J.*, 2014, **20**, 2031–2039.

53 T. Ikeda, K. Sakota and H. Sekiya, *J. Phys. Chem. A*, 2017, **121**, 5809–5816.

54 T. Ikeda, K. Sakota and H. Sekiya, *J. Phys. Chem. A*, 2016, **120**, 1825–1832.

55 K. Sakota, Y. Kouno, S. Harada, M. Miyazaki, M. Fujii and H. Sekiya, *J. Chem. Phys.*, 2012, **137**, 224311.

56 M. Gerhards, A. Jansen, C. Unterberg and A. Gerlach, *J. Chem. Phys.*, 2005, **123**, 074320.

57 M. Gerhards and C. Unterberg, *Appl. Phys. A: Mater. Sci. Process.*, 2001, **72**, 273–279.

58 H. M. Kim, K. Y. Han, J. Park, G. S. Kim and S. K. Kim, *J. Chem. Phys.*, 2008, **128**, 041104.

59 J. Klyne, M. Schmies and O. Dopfer, *J. Phys. Chem. B*, 2014, **118**, 3005–3017.

60 M. Schmies, A. Patzer, M. Schütz, M. Miyazaki, M. Fujii and O. Dopfer, *Phys. Chem. Chem. Phys.*, 2014, **16**, 7980–7995.

61 T. Beyer and D. F. Swinehart, *Commun. ACM*, 1973, **16**, 379.

62 R. H. Page, Y. R. Shen and Y. T. Lee, *J. Chem. Phys.*, 1988, **88**, 4621–4636.

This journal is © the Owner Societies 2022

Phys. Chem. Chem. Phys., 2022, **24**, 73–85 | 85